Chemical Engineering Journal 395 (2020) 125124

Contents lists available at ScienceDirect

Chemical Engineering Journal

journal homepage: www.elsevier.com/locate/cej

Self-adaptive FeP@C nanocages for reversible and long-term lithium-ion batteries

Peng Zhou[a], Qinyou An[a], Shaohua Zhu[a], Kwadwo Asare Owusu[a], Qidong Li[b,c,*], Liqiang Mai[a,d,*]

[a] *State Key Laboratory of Advanced Technology for Materials Synthesis and Processing, Wuhan University of Technology, Wuhan 430070, PR China*
[b] *Engineering Laboratory for Next Generation Power and Energy Storage Batteries, Tsinghua Shenzhen International Graduate School, Shenzhen 518055, PR China*
[c] *Laboratory of Advanced Materials, School of Materials Science and Engineering, Tsinghua University, Beijing 100084, PR China*
[d] *Foshan Xianhu Laboratory of the Advanced Energy Science and Technology Guangdong Laboratory, Xianhu hydrogen Valley, Foshan 528200, PR China*

HIGHLIGHTS

- The FeP@C nanocages are fabricated by the self-template method.
- This Li/FeP@C battery presents high reversible capacity and long-term stability.
- The lithium storage mechanism is confirmed by advanced characterization techniques.

ARTICLE INFO

Keywords:
FeP@C nanocages
Li-ion battery
Fast kinetics
Quantitative analysis
Ex-situ synchrotron HEXRD

ABSTRACT

Till date, the lithium-ion battery still remains the principal and most widely studied rechargeable energy storage device. However, drawbacks including insufficient rate and cycling performance are hindering its further development. The aforementioned drawbacks can be attributed to the unstable interface and sluggish charge storage kinetics of electrode materials. Hence, endowing electrode materials with stable interface and rapid ion/electron diffusion kinetics are effective methods to solve these problems. Herein, by tuning the antihunt interface, a high capacity self-adaptive FeP@C nanocages with fast kinetics are constructed through a self-template method and an etching process. The obtained FeP@C nanocages show a high capacity (~900 mAh g^{-1} at 0.2 A g^{-1}) and superior rate performance (532 mAh g^{-1} at 10 A g^{-1}). Impressively, a stable capacity of 680 mAh g^{-1} is maintained even after a long-term cycling of 800 times at 0.5 A g^{-1}. Moreover, the fast kinetics and lithium storage mechanism are confirmed by quantitative analysis and *ex-situ* synchrotron high energy X-ray diffractions (HEXRD).

1. Introduction

Presently, electricity is one of the most important forms of energy supply in the world [1]. As a carrier of electrical energy, electrochemical energy storage device has become an integral component for efficient use of electrical energy and tremendously improve the equipment performance [2,3]. Li-ion batteries and capacitors are regarded as promising candidates for advanced energy storage as the former possesses the advantage of high energy density while the latter is recognized for its high power performance [4–6]. Compromising the energy density of batteries to achieve high power density or vice-versa in capacitors would result in energy storage systems with insufficient charge-storage mechanisms for emerging fast charging technology and endurance capability of electric devices [7,8]. However, for an exceptional electro-storage device, implementing high capacity and fast charge transfer at the same time is of vital significance. Taking the advantages of batteries and capacitors into account, grafting the fast charge transfer of capacitors to endow battery materials with fast kinetics is an effective way to solve the problem. This will incorporate the effects of both capacitors and batteries and subtly marry the fast kinetics and high capacity via a surface-level and near surface dominated reversible Faradaic reactions, equipping storage devices with high capacity and superior rate performance [9–11].

The fast kinetics in lithium-ion batteries is mainly dependent on the surface and interface of electrode materials during the charge storage process, which is tightly connected with the particle size of the material, reactive sites, stability, ion–electron transmission properties and special field effects [12–18]. Accordingly, many efforts have been

---

[*] Corresponding authors.
E-mail addresses: li_qidong@126.com (Q. Li), mlq518@whut.edu.cn (L. Mai).

https://doi.org/10.1016/j.cej.2020.125124
Received 22 February 2020; Received in revised form 8 April 2020; Accepted 16 April 2020

devoted to exploring effective strategies, such as the synthesis of stable insertion-type electrode materials, the introduction of graphene and carbon nanotubes to form highly conductive composites, and the construction of ordered micro-nanoarrays to improve the material's kinetics [19–23]. Up to now, the typical lithium-ion battery materials with fast kinetics which are described as pseudocapacitive behaviors including $Li_4Ti_5O_{12}$, Nb_2O_5 and TiO_2 have been reported [24–26]. However, the capacitance contributions in these reported materials are mainly realized in form of conventional insertion-type lithium-ion battery electrode materials, which usually have the insuperable defect of low electrochemical capacity. In our understanding, conversion-type lithium-ion battery electrode materials such as sulfides, transition metal oxides and phosphides etc. can provide high electrochemical capacity [27–30]. However, they usually suffer from the unstable interface, poor electronic and ion conductivity, which causes sluggish kinetics. Due to the typical interface effects, a surface-dominated process demonstrates the characteristics of ultra-stability and reversibility [31–34]. Thus, endowing the conversion-type lithium-ion battery electrode materials with antihunt surface and interface to realize fast reaction kinetics will be attractive.

In this work, we fabricated a porous-rich FeP@C nanocages composed of an inner rough-surface FeP nanoparticle, intermediate cushion space, and the outer mesoporous carbon. By thermal treatment and surface-etching process, the as-synthesized FeP@C nanocages possess high surface area, boosting the number of reactive sites to transfer the electrons and ions. Moreover, the typical intermediate cushion spaces create a resistant electrochemical environment to accommodate the drastic pulverization of inner FeP nanoparticle during lithiation and delithiation, while the outer mesoporous carbon supports the formation of a stable SEI layer. Benefiting from the fine design of the structure, the assembled Li/FeP@C half battery presents high reversible capacity (~900 mAh g^{-1} at 0.2 A g^{-1}) and long-term stability with ~680 mAh g^{-1} at 0.5 A g^{-1} over 800 cycles. The conversion reaction was confirmed by *ex-situ* synchrotron HEXRD, and the fast kinetics were proved via quantitative analysis. All these enhancements and evidences demonstrate that the conversion-type FeP@C lithium-ion battery material with fast reaction kinetics was constructed successfully. This work brings up a promising method to make battery materials possess high energy density and power density simultaneously.

2. Experimental section

2.1. Synthesis of precursor Fe_2O_3 nanocubes

Fe_2O_3 nanocubes were synthesized via a simple precipitation method following the reported work [35]. Typically, 50 mL 2.0 M $FeCl_3$ solution was made, and followed by adding the other 50 mL 5.4 M NaOH solution. After stirring for 30 min at 75 °C, the resultant colloidal solution was transferred into 100 mL stainless steel autoclaves lined with Teflon and kept for 5 days at 100 °C. The acquired products were washed with ethanol and deionized water for several times. Finally, the uniform Fe_2O_3 nanocubes were obtained after dring overnight under vacuum at 60 °C.

2.2. Synthesis of FeP@C nanocages

In a typical synthesis, 10 mL deionized water was mixed with 70 mL ethyl alcohol, then 200 mg Fe_2O_3 nanocubes were dispersed in the mixed solution. After continuous ultrasonic stirring in water bath for 10 min, 3 mL $NH_3{\cdot}H_2O$ was added under stirring. Then 100 mg resorcinol was dissolved in the above solution and stirred for another 10 min, followed by adding 140 µL formalin and stirring for 2 h. After washing several times with deionized water and ethanol, the red Fe_2O_3@PFR (Phenol formaldehyde resin) nanocubes were collected. The Fe_3O_4@C nanocubes were synthesized by annealing the Fe_2O_3@PFR nanocubes at 550 °C for 4 h in N_2, the heating rate is 2 °C/min. The calcined products were dispersed in 1 M HCl solution and maintained for different time intervals to obtain the Fe_3O_4@C nanocages. Respectively, the FeP@C-0 without this process and FeP@C-30 for 30 min. Finally, the FeP@C-30 nanocages were obtained after phosphating Fe_3O_4@C nanocages at 500 °C for 4 h. The B-FeP nanocubes were fabricated by directly phosphating the Fe_3O_4 nanocubes with same procedure. The preparation of FeP@C-0 nanocubes is same as FeP@C nanocages just without the etching process by HCl.

2.3. Material characterization

The synchrotron HEXRD patterns were collected at 11-ID-C beamline (Advanced Photon Source), Argonne National Laboratory ($\lambda = 0.11725$ Å). The morphology was characterized by field-emission scanning electron microscopy (FESEM, JEOL-7100F, 20 kV), transmission electron microscopy (TEM) and high-resolution TEM (HR-TEM, FEI TECNAI G2 F20). EDS elementary mappings analyses were collected by TEM-outfitted facility. BET surface areas analysis were performed with a Tristar II 3020 instrument. Raman spectra were collected with a Renishaw INVIA micro-Raman spectroscopy system. Thermogravimetric analysis (TGA) was measured with a Netzsch simultaneous analyzer (STA 449 F5). Electrical conductivities were measured using a ULVAC-RIKO ZEM-3 instrument system at room temperature.

2.4. Electrochemical characterization

Using Li metal foil as anode, the electrochemical performance was collected in CR2016-type coin cells. With the weight ratio (active material: acetylene black: binder (CMC) = 80:15:5), the obtained slurry was coated on Cu foil and dried overnight at 80 °C in vacuum. The working electrode was prepared as small discs with a diameter of 1 cm. The mass loading of active materials was ~1.0 mg cm^{-2}. Electrolyte is 1 M $LiPF_6$ in mixed solution (DMC (dimethyl carbonate): EC (ethylene carbonate) = 1:1, vol%). Galvanostatic charge/discharge measurement was performed with a LAND CT2001A. Cycling voltammetry (CV) was conducted with a CHI 1000C electrochemical workstation. Electrochemical impedance spectroscopy (EIS) was performed using an Autolab potentiostat galvanostat (PGSTAT302N).

3. Results and discussion

From the vivid description of the formation process shown in Fig. 1a, a unique self-template method was used to synthesize the FeP@C nanocages. First, the uniform Fe_2O_3 nanocubes (average size is 200 nm, Fig. S1a) were synthesized via a simple hydrothermal process, serving as the precursor and template. Second, through ammonia assistance in alkaline atmosphere, a polymer layer (PRF) is assembled on the surface of Fe_2O_3 nanocubes via the in-situ polymerization of formaldehyde solution and resorcinol to form the Fe_2O_3@PRF (Fig. S1b). Subsequently, the Fe_2O_3@PRF were treated to an annealing process at 500 °C in N_2 atmosphere to carbonize the PRF and form Fe_3O_4@C nanocubes (Fig. S1c). The X-ray diffraction (XRD) patterns in Fig. S2 obviously demonstrate that the pure phases of the desired materials were acquired, matching well with the standard patterns (No. JCPDS: 01-087-1165 for Fe_2O_3 nanocubes, No. JCPDS: 01-076-0956 for Fe_3O_4 nanocubes and Fe_3O_4@C nanocages). Next, the Fe_3O_4@C nanocages were subjected to an etching treatment to create a cushion space between the inner Fe_3O_4 core and the carbon shell. Typically, the inner Fe_3O_4 core becomes smaller and the surface roughens as the etching treatment proceeding, increasing the cushion space. In this work, the Fe_3O_4@C nanocages with optimum cushion space are obtained with an etching time of 30 min (Fig. S1d). After phosphating with sodium hypophosphite under N_2 atmosphere, the FeP@C nanocages are successfully synthesized.

To demonstrate clearly the advantages of FeP@C nanocages, B-FeP

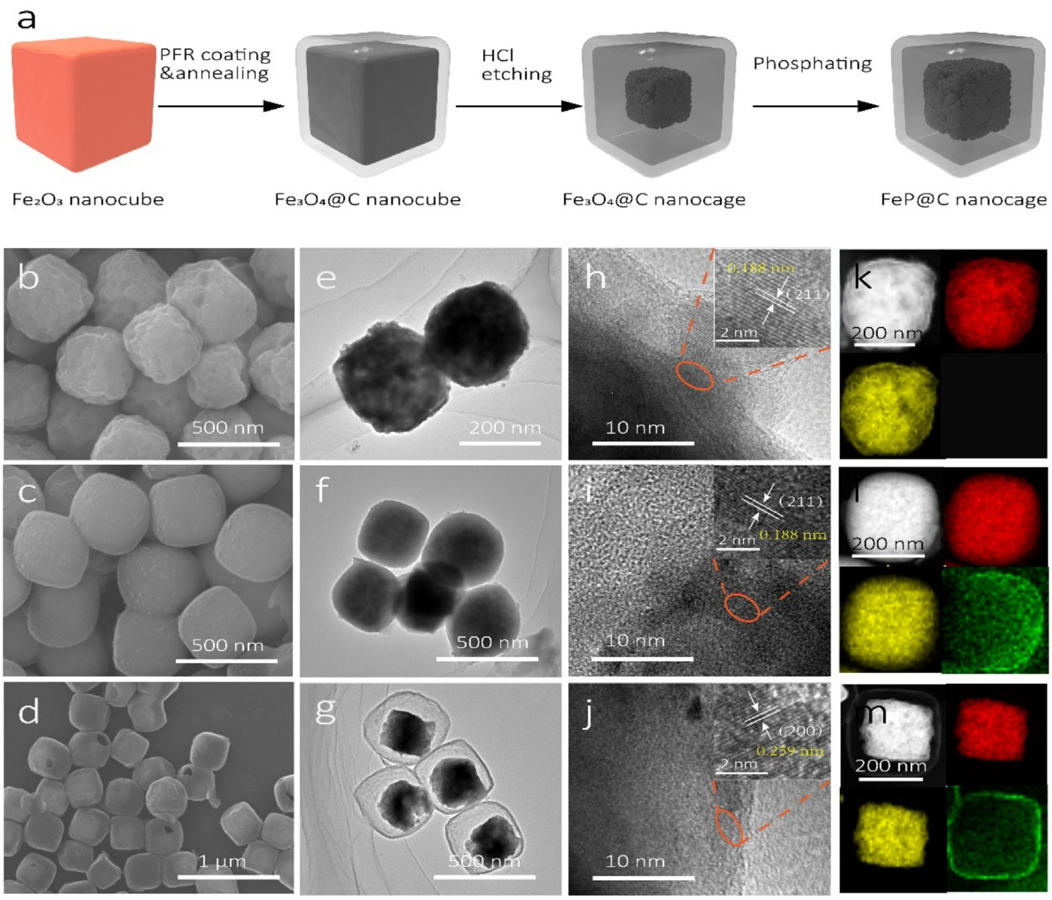

Fig. 1. Schematic illustration of the construction of FeP@C nanocages. (a) FESEM, TEM, HRTEM, HAADF images and EDS elementary mappings of B-FeP nanocubes (b, e, h, k); FeP@C-0 nanocubes (c, f, i, l) and (d, g, j, m) for FeP@C nanocages, respectively.

(bare FeP) and FeP@C-0 were also fabricated. The former does not have both a carbon shell and a cushion space while the latter possesses only a carbon shell. Fig. 1 demonstrates the structural characterization and morphology of these three samples in detail. As depicted in the FESEM image (Fig. 1b), the FeP nanocubes possess a monodisperse morphology with average sizes of 300 nm. Compared with the Fe_3O_4 nanocubes, a rough surface is obtained after the phosphorization of Fe_3O_4 to FeP. This anion-exchange process is expected to generate many pores and interval spaces in FeP. This was further confirmed from the TEM images (Fig. 1e), which also fully agree with observations in other iron-based materials [36,37]. After carbon coating on the rough FeP to obtain the FeP@C-0 nanocubes, the surface became smooth with core–shell like structure (Fig. 1c, f). It is obvious that there is almost no gap between the outer carbon shell and inner FeP core. Next, the SEM and TEM of FeP@C-30 were studied (Fig. 1d, g). The images clearly show that the nanocages are composed of three parts, namely: the inner pore-rich and rough-surface FeP nanoparticle with an average size of 200 nm, appropriate intermediate cushion space (~60 nm), and the outer carbon layer of ~20 nm (Fig. S3). Furthermore, the HR-TEM images display parallel lattice fringes with d-spacing of 1.88 and 2.59 Å, corresponding to FeP (2 1 1) and (2 0 0) crystalline plane, respectively (Fig. 1h-j). Moreover, the elemental analysis of the samples was confirmed by EDS elemental mapping. The corresponding EDS mappings demonstrate that the elemental distributions of Fe and P match well with the structures (Fig. 1k-m). The SEM and TEM results indicate that the FeP@C nanocages have been fabricated successfully through the unique self-template method and a controlled etching process.

Fig. 2a displays the synchrotron HEXRD patterns of the three samples. All the diffraction peaks of B-FeP nanocubes, FeP@C-0 nanocubes and FeP@C-30 nanocages match well with each crystalline plane of the pure FeP (No. JCPDS: 65-2595). As shown in Fig. 2b, the pure FeP possesses an orthorhombic crystal structure (the lattice constants: a = 5.187 Å, b = 3.059 Å, and c = 5.793 Å). In Fig. 2c, the three samples exhibit a type IV isotherm and display a reversible adsorption. This clearly shows that they are mesoporous materials. The B-FeP possesses a specific surface area of 18.79 $m^2\ g^{-1}$, while the inclusion of the carbon coating in FeP@C-0 results in an improved specific surface area of 74.23 $m^2\ g^{-1}$. As is expected, the FeP@C-30 presents the highest BET surface area of 148.23 $m^2\ g^{-1}$ due to the carbon coating and cushion space (~8.2 times that of B-FeP and 2 times that of FeP@C-0). In Fig. S4, the pore size distribution of B-FeP is relatively discrete in the range from 1.7 nm to 15 nm while the pore size of FeP@C-0 is mainly localized at ~2.4 nm. Interestingly, the pore size of FeP@C-30 is localized at ~2.2 and ~19.7 nm, further verifying the mesoporous feature of the carbon layer and the formation of cushion space. The pore structures can also be demonstrated by the TEM images in Fig. 1g. The boosted surface areas and enlarged pore volumes would endow the FeP@C-30 nanocages with more contact interfaces and channels for electrons and ions transmission. Raman spectra of FeP@C-0 and FeP@C-30 were measured to confirm the features of their carbon shells (Fig. 2d). Two apparent peaks which are localized at 1340 cm^{-1} D-band and 1590 cm^{-1} G-band can be obtained for the FeP@C-0 nanocubes and FeP@C-30 nanocages, respectively. TGA is also measured to determine the carbon content of these samples in air atmosphere. The slight weight loss occurring between 350 and 500 °C can be ascribed to the oxidation of carbon while latter gain in weight after 500 °C is due to the oxidation of FeP to Fe_2O_3 and P_2O_5. Via quantitative calculation, the carbon content in FeP@C-0 nanocubes and FeP@C-30 nanocages are assessed to be 7.2% and 18.9 wt%, respectively. Moreover, the FeP@C-30 nanocages exhibits the highest electrical conductivity of

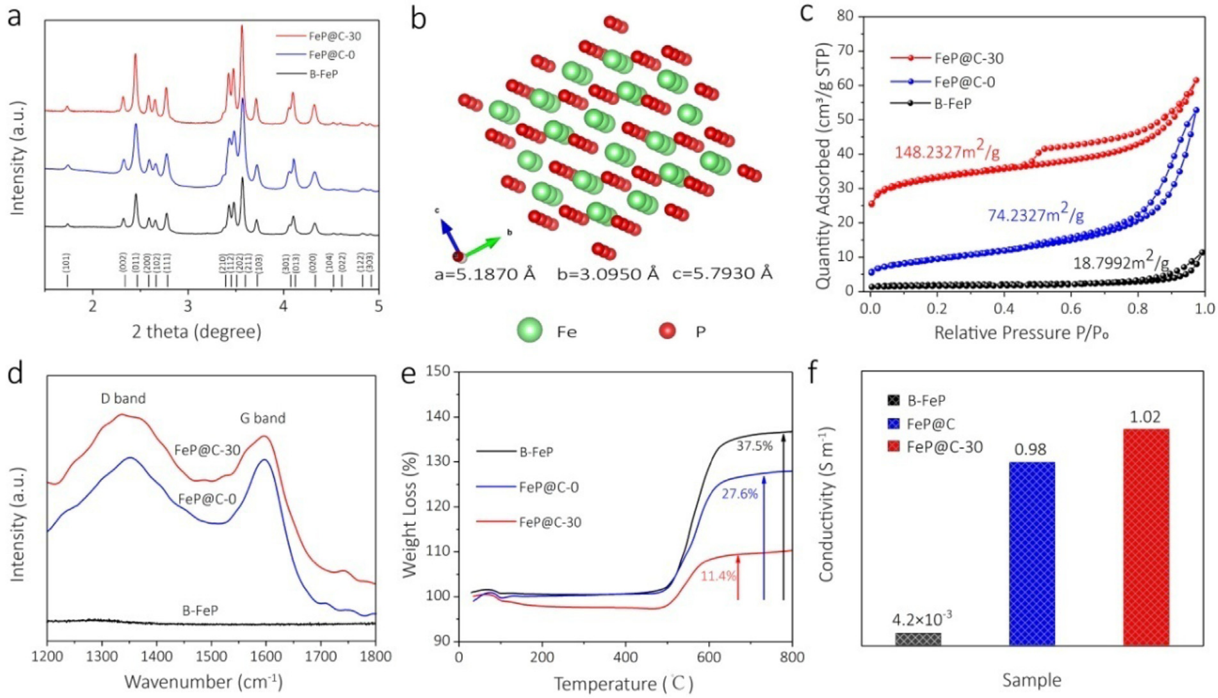

Fig. 2. Detailed structural information of B-FeP, FeP@C-0 and FeP@C-30. (a) Synchrotron HEXRD patterns; (b) crystal structure of FeP; (c) Nitrogen adsorption/desorption isotherms; (d) Raman spectra; (e) TGA curves; (f) The electrical conductivities of B-FeP, FeP@C-0 and FeP@C-30.

~1.02 S m^{-1} in comparison with B-FeP (4.2×10^{-3} S m^{-1}) and FeP@C-0 (0.98 S m^{-1}), which would be advantageous for the reversible transfer of electrons and ions during electrochemical reactions.

To investigate the electrochemical performance for lithium-ion storage, button type-cells are fabricated using the synthesized materials as working electrode. The CV curves of the first three cycles of FeP@C-30 are shown in Fig. 3a and the comparative samples' (FeP@C-0 and FeP) are displayed in Fig. S5. The curves exhibit similar peak shapes apart from the formation of SEI layer in the first discharge process, revealing that the electrochemical reactions are mainly dominated by the FeP phase. In the subsequent cycles, the FeP@C-30 nanocages and the FeP@C-0 nanocubes present stable performances whereas the B-FeP undergo an obvious decay (Fig. S5a) attributed to the drastic pulverization of the structure. The charge/discharge curves for the 1st, 5th and 10th cycles tested at 0.2 A g^{-1} in a voltage range from 0.1 to 3 V (*vs*. Li/Li^+) are displayed in Figs. 3b and S6, respectively, and they show marked variations. The FeP@C-30 nanocages realize the highest capacity with excellent retention. By contrast, the B-FeP shows a low specific capacity and rapid capacity fading while the FeP@C-0 gains some improvements in capacity and cycling stability. The cycling performance of FeP@C and corresponding Fe_3O_4@C is also compared as shown in Fig. S7. It can be seen that the cycling stability of FeP@C is far superior to that of Fe_3O_4@C. The best electrochemical performance observed in the FeP@C-30 is because of the large specific area and stable nanocage structure. Next, the galvanostatic intermittent titration technique (GITT) measurement was performed to investigate the theoretical specific capacity of these samples. The FeP@C-30 nanocages display the highest capacity (Fig. S8). The high capacity (~900 mAh g^{-1}) at a moderate voltage (1.1 V *vs*. Li/Li^+) enables the FeP@C-30 nanocages to be safely applied to high energy storage devices (Fig. 3c). As can be observed in Fig. 3d, the FeP@C-30 nanocages possess the best rate performance, with the highest average capacities of 900, 786, 681, 633, 568 and 532 mAh g^{-1} at current densities of 0.2, 0.5, 1, 2, 5 and 10 A g^{-1}, respectively. When the current density drops back to 0.2 A g^{-1}, the specific capacity correspondingly returns to near 900 mAh g^{-1}. The charge/discharge curves in the rate performance are displayed in Fig. S9. The rate performance of the three samples is shown in Fig. 3d, e. In contrast to the drastic decay in capacities of B-FeP and FeP@C-0 with the increasing current density, the FeP@C-30 displays a more gradual change and reveals the superior reversibility and fast kinetics of the constructed FeP@C-30 nanocages under high current densities. To further investigate its reversibility and fast kinetics, the galvanostatic current discharge (GCD) measurement was applied (Fig. 3f), confirming that the discharge processes exhibit a typical battery behavior. The constructed FeP@C-30 nanocages possess a capacity of 900 mAh g^{-1} within 180 min at 0.2 A g^{-1}. When the current density rises to 1 and 10 A g^{-1}, the discharge time shorten to 63 and 15 min respectively. Impressively, the capacities at 1 and 10 A g^{-1} are 681 (75.7% retention) and 532 mAh g^{-1} (59.1% retention), exhibiting a superior rate performance and huge potential for the fast charging technology.

Disturbances were added during the rate test to ascertain the stability of electrode. It can be observed in Fig. 3g that irrespective of the changes in the current density, once it recovered, the capacity can reach the initial level during the two repetitions within the 200 cycles. The increase of capacity is exhibited in Fig. 3h. The discharge capacity and charge capacity are respectively increased 86.1 mAh g^{-1} and 84.3 mAh g^{-1} at 10 A g^{-1}, indicating an impressive stability and reversibility. The improvement of electric property was also confirmed by CV analysis and EIS after 200 cycles. As shown in Fig. S10, the slight enlargement of the CV area explains the increase in capacity. Both the interfacial layer resistance (R_{suf}) and charge transfer resistance (R_{ct}) appear and display small semi-circles, indicating a stable SEI layer and low R_{ct} of the electrode. The long-term cycling performance is displayed in Fig. 3i and the FeP@C-30 can obtain an initial capacity of 806 mAh g^{-1} at 0.5 A g^{-1}. After a transient activation process, the electrode can stably keep cycling and a 680 mAh g^{-1} (84.5% retention) was maintained for more than 800 cycles, demonstrating a superior stability. As shown in Fig. S11, compared with other typical iron-based battery materials, the FeP@C nanocages exhibit superior rate performance (532 mAh g^{-1} at 10 A g^{-1}) and excellent cycling stability even up to 800 cycles. In contrast, after carbon coating, the FeP@C-0 gains a capacity of 630 mAh g^{-1}; however, the capacity decreases continuously within 120 cycles. This decay is as a result of the absence of the cushion

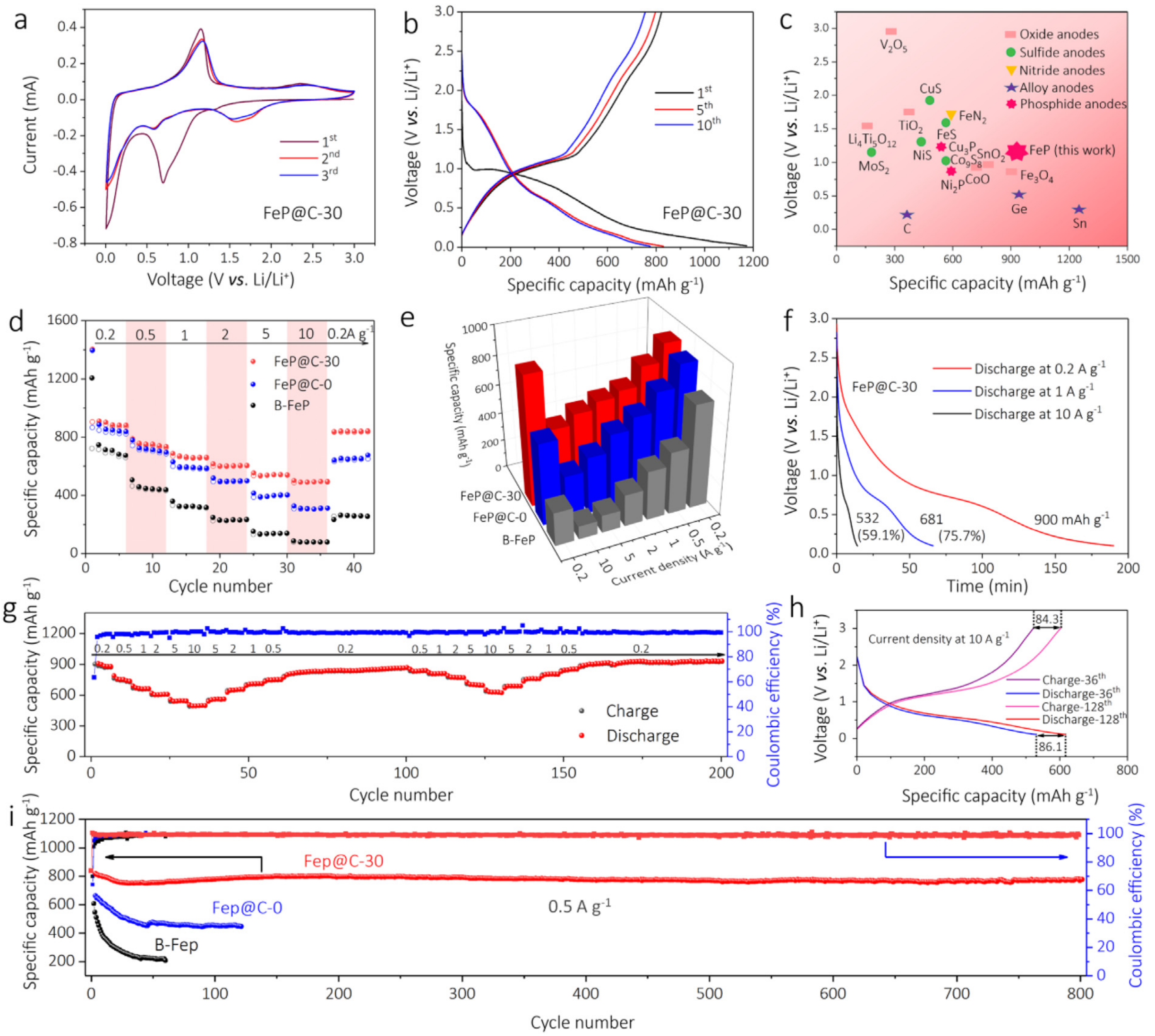

Fig. 3. (a) CV curves of FeP@C nanocages for the first three cycles at the scan rate of 0.2 mV s^{-1}; (b) Charge/discharge curves for the 1st, 5th and 10th cycles at 0.2 A g^{-1}; (c) Comparison of specific capacity related to voltage for typical materials; (d)Rate performance of B-FeP, FeP@C-0, FeP@C-30 and the corresponding 3D column view (e); (f) The GCD of FeP@C-30 nanocages at 0.2, 1 and 10 A g^{-1}; (g) Repeated rate test of FeP@C-30 nanocages with the disturbance adding; (h) The corresponding charge/discharge curves; (i) Cycling performance of B-FeP, FeP@C-0 and FeP@C-30 at 0.5 A g^{-1}.

space to relief the volume change of active FeP and form the stable interface. The B-FeP undergoes a rapid capacity decay, which is mainly attributed to the severe volume changes and the corrosion from the electrolyte in the absence of protected layer.

To further investigate the electrochemical process of FeP@C-30 nanocages electrode, the *ex-situ* synchrotron HEXRD patterns were demonstrated to evaluate the phase evolution of the FeP@C-30 nanocages during the discharge and charge process in the half-cells (Fig. 4a,b). The data points of *ex-situ* synchrotron HEXRD patterns were obtained in the first cycle at 0.1 A g^{-1} at a 2θ range from 2.0 to 5.0°. During the discharge process to 0.01 V, the diffraction peaks matching with the FeP phase are gradually weakened. Instead, the iron crystal (Fe) phase may appear at the same time while the (1 1 0) and (2 0 0) crystal planes at 3.3° and 4.9° increase gradually. In the following charge process to 1.5 and 3 V, the Fe peaks weaken quickly, indicating a reversible conversion type reaction. The TEM of FeP@C after recharge to 3 V is shown in Fig. S12. The TEM image displays parallel lattice fringes with d-spacing of 0.241 nm, corresponding to FeP (1 1 1) crystalline plane. This result further demonstrates the reversibility of FeP. The related reactions could be described as follows:

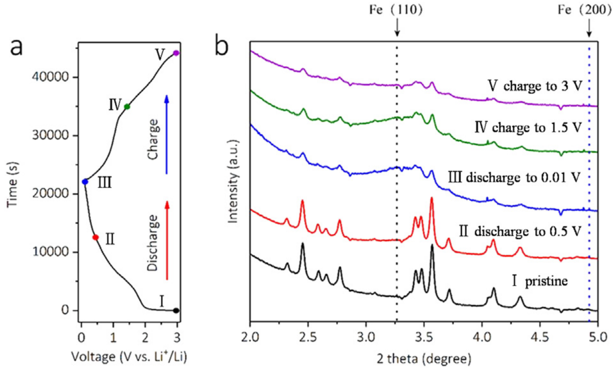

Fig. 4. Charge/discharge curves of FeP@C nanocages at 0.1 A g^{-1} (a) and (b) the corresponding *ex-situ* synchrotron HEXRD patterns.

Discharge process: $FeP + 3Li^{+} + 3e^{-} \rightarrow Fe + Li_3P$

Charge process: $Fe + Li_3P \rightarrow FeP + 3Li^{+} + 3e^{-}$

To further comprehend the greatly enhanced cyclic stability and fast

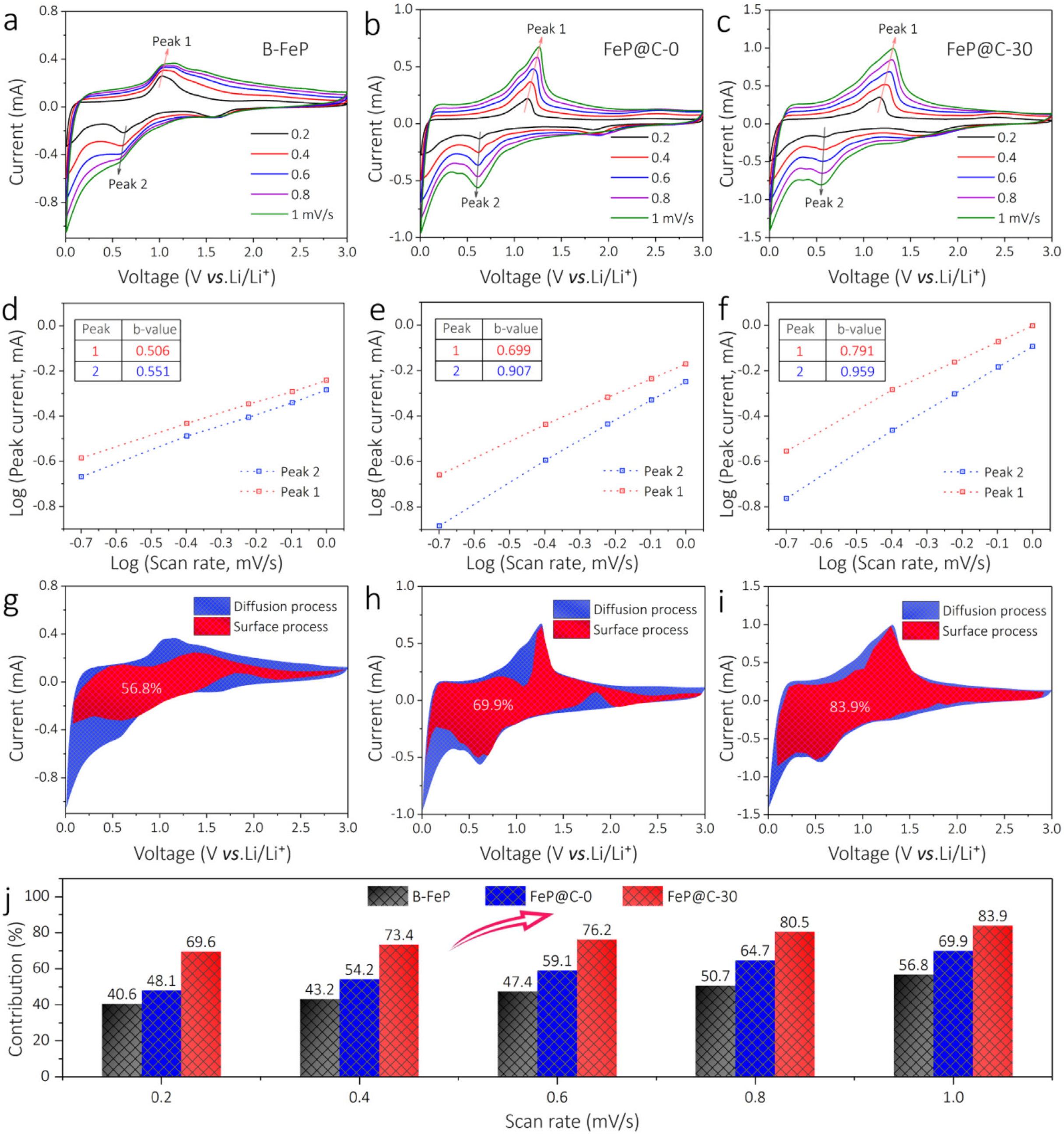

Fig. 5. Quantitative analysis to confirm the kinetics of B-FeP, FeP@C-0 and FeP@C-30. (a–c) CV curves at different scan rates; (d–f) Calculated b-value for the oxidation (peak 1) and reduction (peak 2); (g–i) The separated region of surface process (red) and diffusion process (blue) contribution at 1 mV s^{-1}; (j) Surface process contributions at different scan rates. (For interpretation of the references to colour in this figure legend, the reader is referred to the web version of this article.)

kinetics, detailed quantitative analysis via CV technique measurements was performed. As exhibited in Fig. 5a–c, the CV curves display similar peak positions with slight shifts to high potential with the scan rate increasing from 0.2 to 1 mV s^{-1}, which is the typical feature of the battery materials. Notably, under the same voltage range, the FeP@C-30 nanocages electrode obtained the highest current values and CV areas, which indicates the enhancement of capacity. Here, a generally accepted power-law equation relationship [38] with peak current (*i*) and scan rate (*v*)

$$i = av^b \tag{1}$$

is adopted to quantify the reaction behaviors of B-FeP, FeP@C-0 and FeP@C-30 electrode. In this formula, *a* is a constant and the *b*-value is an estimate of the type of charge transfer of the material. The *b*-value can vary from 0.5 to 1; the *b*-value of 0.5 signifies that the process is dominated by diffusion-controlled while the *b*-value approaching 1 means that the process is the surface-controlled and almost without diffusion resistance. As presented in Fig. 5f, the *b*-values of FeP@C-30 electrode in the oxidation and reduction are 0.791 and 0.959 respectively, indicating the redox reactions are mainly dominated by the fast surface process. Lower *b*-values of the other two samples (Fig. 5d, e) revealed that the reaction in B-FeP electrode was limited by the diffusion process, while the FeP@C-0 exhibited a combined process of surface behavior and diffusion behavior but mainly controlled by the surface behavior. The diffusion resistances were also investigated by EIS in Fig. S13. All the three Nyquist plots display similar semi-circles of charge transfer impedance. Obviously, the FeP@C-30 electrode has the minimum resistance, exhibiting fast R_{ct} and the lowest energy barrier.

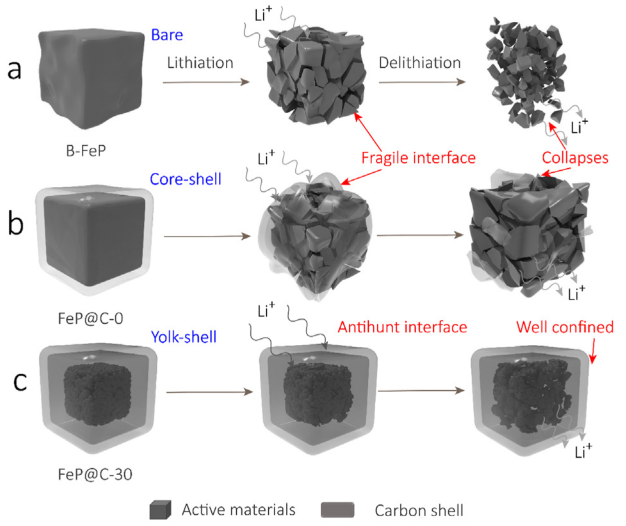

Fig. 6. Structural evolutions during the electrochemical process of (a) B-FeP, (b) FeP@C-0 and (c) FeP@C-30.

The FeP@C-0 has a lower R_{ct} compared to B-FeP, which may be caused by the improvement in conductivity after carbon coating. Based on the EIS results, the Li-ion diffusion coefficients (D) were calculated using the equations [39]:

$$Z_{re} = R_{\Omega} + R_{ct} + \sigma w^{-1/2} \tag{2}$$

$$D = R^2T^2/2A^2n^4F^4C^2\sigma^2 \tag{3}$$

where σ is Warburg factor and can be calculated. Obviously, the smaller σ is, the higher D will be. The slopes (σ) of B-FeP, FeP@C-0 and FeP@C-30 electrodes are 64.59, 53.32 and 48.02 respectively, indicating that the FeP@C-30 has the fastest charge transfer and lowest diffusion barrier. The regions of surface process (k_1v) and diffusion process ($k_2v^{1/2}$) contributions are determined through the following equation [40]:

$$i = k_1v + k_2v^{1/2} \tag{4}$$

As can be observed in Fig. 5g–i, at the scan rate of 1 mV s^{-1}, the FeP@C-30 electrode enables the most surface process contribution of 83.9% which is much higher than that of B-FeP (56.8%) and FeP@C-0 (69.9%) electrode. The surface process contribution of these samples is shown in Fig. 5j. As the scan rate increases, the contribution value also increases. The contribution of FeP@C-30 nanocage electrode is the highest, exhibiting the fast charge transfer property of the constructed nanocage structure.

The structure evolution during the electrochemical process is displayed in Fig. 6 and demonstrated by the *ex-situ* SEM images in Fig. S14. For the B-FeP, due to the absence of a protective layer, the drastic volume expansion leads to the easy destruction of the structure which exposes the active particles to be corroded by the electrolyte. This causes them to fall off from the electrode within 10 cycles and makes it difficult to form the stable SEI, which also explains the continuous capacity fading in Fig. 3i. Even though the FeP@C-0 gains an improvement in capacity after the carbon layer coating, the capacity fading still exists owing to the lack of cushion space to buffer the severe volume change. The volume expansion causes a strain on the carbon layer, resulting in the ultimate failure of the structure. Many broken carbon sheets can be clearly seen on the surface of FeP cores after 50 cycles in Fig. S14b, indicating the failure of the core–shell structure. Benefiting from the unique nanocages design, the FeP@C-30 nanocages not only possess the antihunt carbon layer to form the stable interface, but the sufficient cushion space can greatly buffer the expansion stress from the inner active FeP yolk, thus confining the structure well. The structure is well maintained even after 200 cycles as shown in Fig. S14c.

4. Conclusion

In summary, the self-adaptive FeP@C nanocages have been successfully fabricated using the self-template method and a surface etching process. This novel nanocage structure boosts the lithium-ion storage properties by improving the ion/electron transfer kinetics and stability of the active materials. As anode material for lithium-ion battery, the FeP@C nanocages present fast kinetics, high reversible capacity (~900 mAh g^{-1} at 0.2 A g^{-1}) and long-term stability with ~680 mAh g^{-1} over 800 cycles at 0.5 A g^{-1}. Quantitative analysis and stability testing further confirm the fast kinetics and the stable feature of this structure. This work brings up a promising method to endow the sluggish electrode materials with stable structures and enable them with high energy density and rate performance simultaneously.

Declaration of Competing Interest

The authors declare that they have no known competing financial interests or personal relationships that could have appeared to influence the work reported in this paper.

Acknowledgements

This work was supported by the National Key Research and Development Program of China (2016YFA0202603), the National Natural Science Foundation of China (51832004, 51521001), the Programme of Introducing Talents of Discipline to Universities (B17034), the Yellow Crane Talent (Science & Technology) Program of Wuhan City, Foshan Xianhu Laboratory of the Advanced Energy Science and Technology Guangdong Laboratory (XHT2020-003). This research used resources of the Advanced Photon Source (11ID-C), a U.S. Department of Energy (DOE) Office of Science User Facility operated for the DOE Office of Science by Argonne National Laboratory under Contract No. DE-AC02-06CH11357.

Appendix A. Supplementary data

Supplementary data to this article can be found online at https://doi.org/10.1016/j.cej.2020.125124.

References

[1] S. Chu, A. Majumdar, Opportunities and challenges for a sustainable energy future, Nature 488 (2012) 294–303, https://doi.org/10.1038/nature11475.
[2] B. Kang, G. Ceder, Battery materials for ultrafast charging and discharging, Nature 458 (2009) 190–193, https://doi.org/10.1038/nature07853.
[3] S. Chu, Y. Cui, N. Liu, The path towards sustainable energy, Nat. Mater. 16 (2016) 16–22, https://doi.org/10.1038/nmat4834.
[4] D.P. Tabor, L.M. Roch, S.K. Saikin, C. Kreisbeck, D. Sheberla, J.H. Montoya, S. Dwaraknath, M. Aykol, C. Ortiz, H. Tribukait, C. Amador-Bedolla, C.J. Brabec, B. Maruyama, K.A. Persson, A. Aspuru-Guzik, Accelerating the discovery of materials for clean energy in the era of smart automation, Nat. Rev. Mater. 3 (2018) 5–20, https://doi.org/10.1038/s41578-018-0005-z.
[5] C.M. Park, J.H. Kim, H. Kim, H. Sohn, Li-alloy based anode materials for Li secondary batteries, Chem. Soc. Rev. 39 (2010) 3115–3141, https://doi.org/10.1039/b919877f.
[6] W. Luo, X. Chen, Y. Xia, M. Chen, L. Wang, Q. Wang, W. Li, J. Yang, Surface and interface engineering of silicon-based anode materials for lithium-ion batteries, Adv. Energy Mater. 7 1701083 (2017), https://doi.org/10.1002/aenm.201701083.
[7] P. Simon, Y. Gogotsi, B. Dunn, Where do batteries end and supercapacitors begin, Science 343 (2014) 1210–1211, https://doi.org/10.1126/science.1249625.
[8] V. Augustyn, P. Simon, B. Dunn, Pseudocapacitive oxide materialsfor high-rate electrochemical energy storage, Energy Environ. Sci. 7 (2014) 1597–1614, https://doi.org/10.1039/C3EE44164D.
[9] D. Chao, C. Zhu, P. Yang, X. Xia, J. Liu, J. Wang, X. Fan, S.V. Savilov, J. Lin, H.J. Fan, Z.X. Shen, Array of nanosheets render ultrafast and high-capacity Na-ion storage by tunable pseudocapacitance, Nat. Commun. 7 (2016) 1–8, https://doi.org/10.1038/ncomms12122.
[10] X. Xu, R. Zhao, B. Chen, L. Wu, C. Zou, W. Ai, H. Zhang, W. Huang, T. Yu, Progressively exposing active facets of 2D nanosheets toward enhanced pseudocapacitive response and high-rate sodium storage, Adv. Mater. 31 (2019) 1900526, https://doi.org/10.1002/adma.201900526.

[11] D. Luo, J. Xu, Q. Guo, L. Fang, X. Zhu, Q. Xia, H. Xia, Surface-dominated sodium storage towards high capacity and ultrastable anode material for sodium-ion batteries, Adv. Funct. Mater. 28 (2018) 1805371, https://doi.org/10.1002/adfm.201805371.

[12] W. Luo, Y. Wang, L. Wang, W. Jiang, S. Chou, S. Dou, H. Liu, J. Yang, Silicon/mesoporous carbon/crystalline TiO_2 nanoparticles for highly stable lithium storage, ACS Nano. 10 (2016) 10524–10532, https://doi.org/10.1021/acsnano.6b06517.

[13] Y. Qi, Y. Lu, F. Ding, Q. Zhang, H. Li, X. Huang, L. Chen, Y.S. Hu, Slope-dominated carbon anode with high specific capacity and superior rate capability for high safety Na-ion Batteries, Angew. Chem. Int. Edit. 58 (2019) 4361–4365, https://doi.org/10.1002/anie.201900005.

[14] J. Wang, J. Polleux, J. Lim, B. Dunn, Pseudocapacitive contributions to electrochemical energy storage in TiO_2 (Anatase) nanoparticles, J. Phys. Chem. C 111 (2007) 14925–14931, https://doi.org/10.1021/jp074464w.

[15] Q. Li, L. Li, K.A. Owusu, W. Luo, Q. An, Q. Wei, Q. Zhang, L. Mai, Self-adaptive mesoporous CoS@alveolus-like carbon yolk-shell microsphere for alkali cations storage, Nano Energy 41 (2017) 109–116, https://doi.org/10.1016/j.nanoen.2017.09.022.

[16] Z. Liu, X.-Y. Yu, X.W. Lou, U. Paik, Sb@C coaxial nanotubes as a superior long-life and high-rate anode for sodium ion batteries, Energy Environ. Sci. 9 (2016) 2314–2318, https://doi.org/10.1039/C6EE01501H.

[17] C. Guan, X. Li, Z. Wang, X. Cao, C. Soci, H. Zhang, H.J. Fan, Nanoporous walls on macroporous foam: rational design of electrodes to push areal pseudocapacitance, Adv. Mater. 24 (2012) 4186–4190, https://doi.org/10.1002/adma.201104295.

[18] J. Hu, Y. Jiang, S. Cui, Y. Duan, T. Liu, H. Guo, L. Lin, Y. Lin, J. Zheng, K. Amine, F. Pan, 3D-printed cathodes of $LiMn_{1-x}Fe_xPO_4$ nanocrystals achieve both ultrahigh rate and high capacity for advanced lithium-ion battery, Adv. Energy Mater. 6 (2016) 1600856, https://doi.org/10.1002/aenm.201600856.

[19] S.R. Peurifoy, J.C. Russell, T.J. Sisto, Y. Yang, X. Roy, C. Nuckolls, Designing three-dimensional architectures for high-performance electron accepting pseudocapacitors, J. Am. Chem. Soc. 140 (2018) 10960–10964, https://doi.org/10.1021/jacs.8b07365.

[20] J. Guo, X. Du, X. Zhang, F. Zhang, J. Liu, Facile formation of a solid electrolyte interface as a smart blocking layer for high-stability sulfur cathode, Adv. Mater. 29 (2017) 1700273, https://doi.org/10.1002/adma.201700273.

[21] H.T. Sun, M. Lin, J.F. Liang, Z.P. Zhao, C. Lee, H.L. Fei, M.N. Ding, J. Lau, M.F. Li, C. Wang, X. Xu, G.L. Hao, B. Papandrea, I. Shakir, B. Dunn, Y. Huang, X.F. Duan, Three-dimensional holey-graphene/niobia composite architectures for ultrahigh-rate energy storage, Science 356 (2017) 599–604, https://doi.org/10.1126/science.aam5852.

[22] Y.-H. Zhu, X. Yang, D. Bao, X.-F. Bie, T. Sun, S. Wang, Y.-S. Jiang, X.-B. Zhang, J.-M. Yan, Q. Jiang, High-energy-density flexible potassium-ion battery based on patterned electrodes, Joule 2 (2018) 736–746, https://doi.org/10.1016/j.joule.2018.01.010.

[23] G. Fang, Z. Wu, J. Zhou, C. Zhu, X. Cao, T. Lin, Y. Chen, C. Wang, A. Pan, S. Liang, Observation of pseudocapacitive effect and fast ion diffusion in bimetallic sulfides as an advanced sodium-ion battery anode, Adv. Energy Mater. 8 (2018) 1703155, https://doi.org/10.1002/aenm.201703155.

[24] V. Augustyn, J. Come, M.A. Lowe, J.W. Kim, P.L. Taberna, S.H. Tolbert, H.D. Abruna, P. Simon, B. Dunn, High-rate electrochemical energy storage through Li^+ intercalation pseudocapacitance, Nat. Mater. 12 (2013) 518–522, https://doi.org/10.1038/NMAT3601.

[25] J. Yang, Y. Wang, W. Li, L. Wang, Y. Fan, W. Jiang, W. Luo, Y. Wang, B. Kong, C. Selomulya, H.K. Liu, S.X. Dou, D. Zhao, Amorphous TiO2 shells: a vital elastic buffering layer on silicon nanoparticles for high-performance and safe lithium storage, Adv. Mater. 29 (2017) 1700523, https://doi.org/10.1002/adma.201700523.

[26] E. Lim, C. Jo, H. Kim, M. Kim, Y. Mun, J. Chun, Y. Ye, J. Hwang, K. Ha, C. Kwang, K. Kang, S. Yoon, J. Lee, Facile synthesis of Nb2O5@carbon core-shell nanocrystals with controlled crystalline structure for high-power anodes in hybrid supercapacitors, ACS Nano. 9 (2015) 7497–7505, https://doi.org/10.1021/acsnano.5b02601.

[27] D. Li, D. Yang, X. Yang, Y. Wang, Z. Guo, Y. Xia, S. Sun, S. Guo, Double-helix structure in carrageenan-metal hydrogels: a general approach to porous metal sulfides/carbon aerogels with excellent sodium-ion storage, Angew. Chem. Int. Edit. 55 (2016) 15925–15928, https://doi.org/10.1002/ange.201610301.

[28] Y. Lu, N. Zhang, S. Jiang, Y. Zhang, M. Zhou, Z. Tao, L.A. Archer, J. Chen, High-capacity and ultrafast Na-ion storage of a self-supported 3D porous antimony Persulfide@Graphene foam architecture, Nano Lett. 17 (2017) 3668–3674, https://doi.org/10.1021/acs.nanolett.7b00889.

[29] W. Zhang, W.K. Pang, V. Sencadas, Z. Guo, Understanding high-energy-density Sn_4P_3 anodes for potassium-ion batteries, Joule 2 (2018) 1534–1547, https://doi.org/10.1016/j.joule.2018.04.022.

[30] G. Tan, R. Xu, Z. Xing, Y. Yuan, J. Lu, J. Wen, C. Liu, L. Ma, C. Zhan, Q. Liu, T. Wu, Z. Jian, R. Shahbazian-Yassar, Y. Ren, D.J. Miller, L.A. Curtiss, X. Ji, K. Amine, Burning Lithium in CS_2 for high-performing compact Li_2S-graphene nanocapsules for Li–S batteries, Nat. Energy 2 (2017) 17090, https://doi.org/10.1038/nenergy.2017.90.

[31] C. Ye, L. Zhang, C. Guo, D. Li, A. Vasileff, H. Wang, S.-Z. Qiao, A 3D hybrid of chemically coupled nickel sulfide and hollow carbon spheres for high performance lithium-sulfur batteries, Adv. Funct. Mater. 27 (2017) 1702524, https://doi.org/10.1002/adfm.201702524.

[32] M.R. Kaiser, Z. Ma, X. Wang, F. Han, T. Gao, X. Fan, J.Z. Wang, H.K. Liu, S. Dou, C. Wang, Reverse microemulsion synthesis of sulfur/graphene composite for lithium/sulfur batteries, ACS Nano 11 (2017) 9048–9056, https://doi.org/10.1021/acsnano.7b03591.

[33] Z. Sun, J. Zhang, L. Yin, G. Hu, R. Fang, H.M. Cheng, F. Li, Conductive porous vanadium nitride/graphene composite as chemical anchor of polysulfides for lithium-sulfur batteries, Nat. Commun. 8 (2017) 1–8, https://doi.org/10.1038/ncomms14627.

[34] F. Pei, L. Lin, D. Ou, Z. Zheng, S. Mo, X. Fang, N. Zheng, Self-supporting sulfur cathodes enabled by two-dimensional carbon yolk-shell nanosheets for high-energy-density lithium-sulfur batteries, Nat. Commun. 8 (2017) 1–10, https://doi.org/10.1038/s41467-017-00575-8.

[35] X. Wang, K. Chen, G. Wang, X. Liu, H. Wang, Rational design of three-dimensional graphene encapsulated with hollow FeP@Carbon nanocomposite as outstanding anode material for lithium ion and sodium ion batteries, ACS Nano 11 (2017) 11602–11616, https://doi.org/10.1021/acsnano.7b06625.

[36] Y. Dong, B. Wang, K. Zhao, Y. Yu, X. Wang, L. Mai, S. Jin, Air-stable porous Fe_2N encapsulated in carbon microboxes with high volumetric lithium storage capacity and a long cycle life, Nano Lett. 17 (2017) 5740–5746, https://doi.org/10.1021/acs.nanolett.7b02698.

[37] Z. Liu, T. Lu, T. Song, X.-Y. Yu, X.W. Lou, U. Paik, Structure-designed synthesis of FeS_2@C yolk–shell nanoboxes as a high-performance anode for sodium-ion batteries, *Energy. Environ. Sci.* 10 (2017) 1576–1580, https://doi.org/10.1039/c7ee01100h.

[38] P. He, M. Yan, G. Zhang, R. Sun, L. Chen, Q. An, L. Mai, Layered VS_2 nanosheet-based aqueous Zn ion battery cathode, Adv. Energy Mater. 7 (2017) 1601920, https://doi.org/10.1002/aenm.201601920.

[39] Q. Li, L. Li, P. Wu, N. Xu, L. Wang, M. Li, A. Dai, K. Amine, L. Mai, J. Lu, Silica restricting the sulfur volatilization of nickel sulfide for high-performance lithium-ion batteries, Adv. Energy Mater. 9 (2019) 1901153, https://doi.org/10.1002/aenm.201901153.

[40] Q. Li, Q. Wei, Q. Wang, W. Luo, Q. An, Y. Xu, C. Niu, C. Tang, L. Mai, Self-template synthesis of hollow shell-controlled Li_3VO_4 as a high-performance anode for lithium-ion batteries, J. Mater. Chem. A 3 (2015) 18839–18842, https://doi.org/10.1039/c5ta05594f.